Temperature- and ligand-dependent carrier transport dynamics in photovoltaic PbS colloidal quantum dot thin films using diffusion-wave methods

CrossMark

Lilei Hu[a], Andreas Mandelis[a,b,c,*], Zhenyu Yang[b], Xinxin Guo[a], Xinzheng Lan[b], Mengxia Liu[b], Grant Walters[b], Alexander Melnikov[a], Edward H. Sargent[b]

[a] Center for Advanced Diffusion-Wave and Photoacoustic Technologies (CADIPT), Department of Mechanical and Industrial Engineering, University of Toronto, Toronto, Ontario, Canada M5S 3G8
[b] Edward S. Rogers Sr. Department of Electrical and Computer Engineering, University of Toronto, Toronto, Ontario, Canada M5S 3G4
[c] School of Optoelectronic Information, University of Electronic Science and Technology of China, Chengdu, Sichuan, 610054, China

ARTICLE INFO

ABSTRACT

Solution-processed colloidal quantum dots (CQDs) are promising candidates for large-scale, low-cost, and lightweight photovoltaic and electronic devices. Carrier transport dynamics has a substantial impact on device efficiency optimization. Coupled with photocarrier radiometry (PCR) — a dynamic spectrally integrated frequency-domain photoluminescence (PL) modality, we report the derivation of a trap-state-mediated carrier hopping transport model for the extraction of multiple carrier transport parameters in PbS CQD thin films. These parameters, including effective carrier lifetime τ_E, hopping diffusivity D_h, trap-state-dependent carrier trapping rate R_T, diffusion length L_h, and carrier thermal emission rate e_i, were obtained for CQD thin films with different dot size and capping ligands: tetrabutylammonium iodide (TBAI), 1,2-ethanedithiol (EDT), and methylammonium lead triiodide perovskite (MAPbI$_3$). Consistent with the framework of phonon-assisted carrier hopping mechanism, τ_E, D_h, and L_h have demonstrated a monotonic dependence on temperature in the range from 100 K to 300 K. Perovskite-passivated PbS CQD thin films, especially those with larger dot sizes which are free of apparent defect induced PL emission and have higher τ_E and D_h at room temperature (ca. 0.51 μs and 1.80×10^{-2} cm^2/s, respectively) than their counterparts, demonstrate better photovoltaic material properties. Dot-size-dependent exciton binding energies (35.21–53.20 meV) were characterized using a dynamic PCR photo-thermal spectroscopy that also characterized the trap-state-mediated carrier hopping activation energies in the range from 100 meV to 280 meV. To test the reliability of the best-fitted results, computational fitting uniqueness was examined using a parametric theory.

1. Introduction

Solution-processed colloidal quantum dots (CQDs) have appealing electronic and optical properties such as size-tunable energy bandgap [1,2], multiple exciton generation [3–5], pathways for harvesting hot-electrons [6], and ambipolar (hole and electron) charge transfer [7,8]. Due to these unique granular electronic material features, CQDs have shown great potentials in various optoelectronic and electronic device applications, including thin films transistors [9–11], photodetectors [3,12–14], solar cells [15–18], and light-emitting diodes [19,20].

Understanding carrier transport dynamics and shedding light on energy dissipation mechanisms in optoelectronics is essential to device efficiency optimization. QD disorder in the form of energy and/or geometry, originating in dot shape, size, composition, surface chemistry, and capping ligands, as well as the degree of polydispersity and superlattice order in thin films, disrupts the formation of continuous energy band structures in CQD ensembles. Depending on the level of QD disorder, there are four possible carrier transport mechanisms [21]: (i) bulk crystal-like Bloch state electron transport, (ii) direct tunneling mechanisms without the help of phonons, (iii) over-the-barrier carrier activation, and (iv) phonon-assisted hopping. Phonon-assisted hopping in the form of, for example, nearest neighbor hopping (NNH) and Efros-Shklovskii variable range hopping (ES-VRH), is the most prevailing mechanism that has been widely applied in studying

* Corresponding author at: Center for Advanced Diffusion-Wave and Photoacoustic Technologies (CADIPT), Department of Mechanical and Industrial Engineering, University of Toronto, Toronto, Ontario, Canada M5S 3G8.
E-mail address: mandelis@mie.utoronto.ca (A. Mandelis).

various QD systems [22–28] in which carriers hop from one dot to the next depending on the interdot distance, coupling strength, temperature, and the type of carrier. Moreover, strengthening the capping-ligand-controlled interdot coupling has been reported in PbSe QDs as originating in the Coulomb blockade dominated insulating regime and into the hopping conduction dominated semiconductor regime [22], and has also been found to assist exciton dissociation into free electrons and holes [29,30]. Furthermore, Lee et al. [31] and Liu et al. [24] have observed a monotonic increase in hole mobility with increasing QD size, while electron mobility exhibits a peak at QD diameter of 6 nm, which can be ascribed to the compromise between reduced activation energy (lower hopping energy barrier) and weakened interdot coupling strength amongst larger QDs. In addition, hopping conduction behavior has been manifested when carrier mobility drops exponentially with the increase of capping ligand length [24], showing consistency with the Shklovskii and Efros hopping mobility equation [32]. The phonon-assisted hopping transport mechanism predicts a temperature-dependent carrier mobility, diffusivity, lifetime, conductivity, and conductance of QD devices [18,22,23,25,27,28,33]. However, due to the large specific surfaces of QDs, even with the application of capping ligands, QD trap states still hinder the efficiency of CQD based electronic devices through acting as undesired radiative and nonradiative recombination centers [24,34–40]. Important as these effects are, a systematic study of trap-state-modified carrier transport is still lacking.

Despite the importance of carrier dynamics to QD optoelectronic and electronic device efficiency optimization, current characterization techniques are still not able to provide sufficient feedback information about carrier transport kinetics in QD substrates and devices. At present, carrier mobility can be characterized by linearly increasing voltage (CELIV) [39,41,42], time of flight (TOF) [41,43], transient photovoltage [39,44], and by using field effect transistors (FET) [39,45,46]. Nonetheless, these methods require thick QD films and a completed device. Although Zhitomirsky et al. [47] introduced photo-luminescence (PL) quenching for carrier diffusion length measurement in CQD thin films, additional coating and/or embedding different types of CQDs are compulsory. Nowadays, carrier lifetime is measured mostly by V_{oc} (open-circuit voltage) transient decay [41] and transient PL [39,48,49] for devices and substrates, respectively. However, due to the fragile nature of materials comprising photovoltaic devices, especially organic and QD-based solar cells, most of these conventional techniques are suitable neither for industrial in-line mass manufacturing of electronic devices at any and all fabrication stages, nor for optoelectronic process analysis involving light-carrier interactions.

In view of these facts, this paper introduces an all-optical, fast, and non-destructive technique, photocarrier radiometry (PCR)—a dynamic spectrally integrated frequency-domain PL modality, to the characterization of CQD thin films. A trap-state-mediated carrier hopping transport model was developed and applied for the extraction of multiple carrier transport parameters of different ligand-capped PbS CQD thin films. The temperature-dependent carrier transport dynamics was investigated in perovskite-passivated PbS CQD thin films. Furthermore, sample homogeneity was examined through PCR-based lock-in carrierography (LIC) imaging [50]. The energy band structure and carrier transport activation energies of our CQD thin films were analyzed using static PL and photo-thermal spectroscopy (PTS) [51], respectively. Combined with a carrier hopping transport model, PCR was shown to exhibit great potential in QD materials characterization for fundamental physics research of carrier transport dynamics, in addition to being an all-optical, nondestructive and promising technique for industrial device quality control.

2. Carrier hopping transport model

Fig. 1(a) and (b) exhibit the schematic of surface-passivated and laser-illuminated PbS CQDs in a ligand matrix. Upon laser excitation,
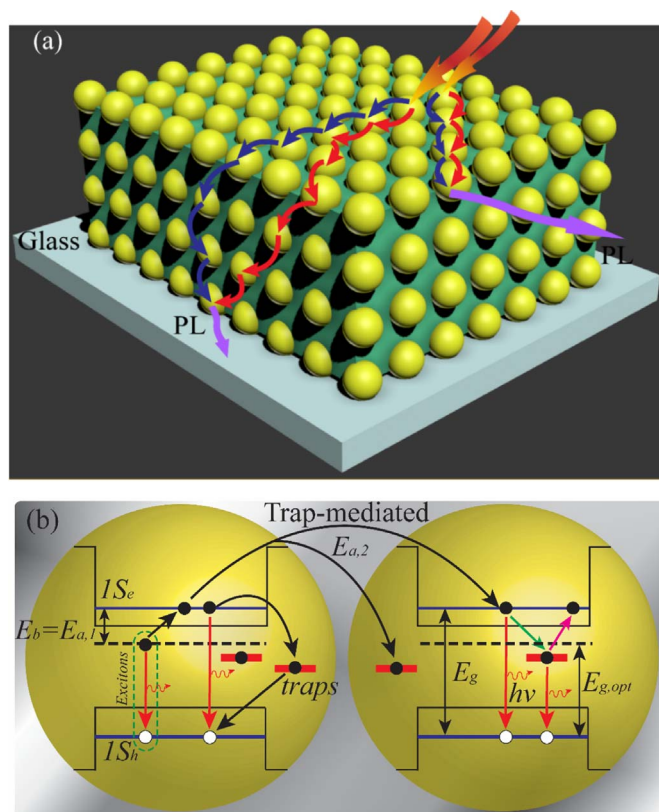

Fig. 1. (a) Schematic of carrier hopping transport in PbS CQD thin films embedded in a surface-passivation ligand matrix when excited by a frequency-modulated laser source. (b) Illustration of carrier generation, dissociation, hopping transport, and trapping processes in a CQD assembly. S_e and S_h are the ground states for electrons and holes, respectively. $E_{a,1}$ and $E_{a,2}$ are the activation energies associated with exciton binding energy (E_b) and trap-mediated transition process, respectively. E_g and $E_{g,\ opt}$ are, respectively, the electronic and optical band gap energy.

excitons will firstly form within the CQDs and diffuse away through a carrier hopping mechanism [Fig. 1(a)], during which process, excitons may dissociate into free charge carriers. All these particles, including excitons and their dissociated charge carriers can recombine radiatively, or be bound to or trapped in trap states and recombine radiatively or non-radiatively [Fig. 1(b)]. The rate equation for the population $N_i(x, t)$ of charge carriers in quantum dot i [52] must include the presence of trap states acting as thermal emission and capture centers. Such trap states have been reported in thiol-capped PbS QDs [53], and in glass-encapsulated PbS QDs [54], also several trap-related emission bands have been reported for PbS QDs in polyvinyl alcohol [55]. Taking into consideration that those trap states acting as thermal emission and capture centers, the carrier rate equation can be expressed as:

$$\frac{\partial N_i(x, t)}{\partial t} = -\sum_j P_{ij} N_i(x, t) + \sum_j P_{ji} N_j(x, t)$$
$$+ \sum_{k=1}^{m} \{e_{ik}(T) n_{Tk}(x, t) - C_{ik} N_i(x, t)[N_{Tk} - n_{Tk}(x, t)]\} - \frac{N_i(x, t)}{\tau}$$
$$+ G_0(x, t) \tag{1}$$

where k denotes trap level, e_{ik} is the thermal emission rate of charge carriers from the trap level k, C_{ik} is the charge carrier capture coefficient, τ is the carrier lifetime, N_{Tk} is the trap density of level k, n_{Tk} is the trapped carrier density, P_{ij} (P_{ji}) is the hopping probability from the i_{th} (j_{th}) QD to the j_{th}(i_{th}) QD. Here, $C_{ik} N_{Tk}$ is defined as the carrier-trapping rate R_{Tk}. G_0 is the photocarrier generation rate. In the PbS CQD system under consideration, all the trap states at different levels are considered to have the same effects on carrier transport behavior,

i.e. trapping and detrapping carriers. Although distinguishing them is possible using photo-thermal deep level transient spectroscopy at various temperatures and can yield a more detailed structure of trap levels, however, it is not necessary for the present optoelectronic transport property characterization. Therefore, the rate equation for carrier population can be further developed to

$$\frac{\partial N_i(x, t)}{\partial t} = -\frac{\partial J_e(x, t)}{\partial x} + e_i(T)n_T(x, t) - C_i N_i(x, t)[N_T - n_T(x, t)] - \frac{N_i(x, t)}{\tau}$$
$$+ G_0(x, t) \tag{2}$$

where the charge carrier current density $J_e(x, t)$ is a function of the hopping diffusivity D_h and can be written as

$$J_e(x, t) = -D_h(T)\frac{\partial N_i(x, t)}{\partial x} \tag{3}$$

Hopping diffusivity D_h is a fundamental photovoltaic electronic property, which depends on the interdot distance L, charge carrier hopping probability γ, and temperature T, through the following relationship:

$$D_h(T) = \frac{L^2}{\tau_0}e^{-\gamma L - \Delta E_{ji}/k_B T} \tag{4}$$

where τ_0 is the hopping time of a carrier from one QD to another, γ is the hopping transmission coefficient, L is the effective interdot distance, T is the temperature, ΔE_{ji} is the energy difference of a hopping particle (exciton or dissociated carrier) between QD states (i) and (j) [56], and k_B is the Boltzmann constant. Since trapped charge carriers (n_T) can be emitted from trap states or re-captured, the kinetic equation for n_T is given by

$$\frac{\partial n_T(x, t)}{\partial t} = -e_i(T)n_T(x, t) + C_i N_i(x, t)[N_T - n_T(x, t)] \tag{5}$$

Combining Eqs. (2)–(5) yields an expression for the kinetics of the carrier population in a QD ensemble involving the charge carrier generation, capture, and release from trap states, as well as the carrier hopping diffusion:

$$\frac{\partial N_i(x, t)}{\partial t} + \left\{ C_i[N_T - n_T(x, t)] + \frac{1}{\tau(T)} \right\} N_i(x, t) = G_0(x, t; \omega) + e_i(T)n_T(x, t)$$
$$+ D_h(T)\frac{\partial^2 N_i(x, t)}{\partial x^2} \tag{6}$$

There is much evidence for the existence of bright (or singlet) and dark (or triplet) states in PbS QDs [54,57–59]. Non-radiative recombination processes arise from charge carriers trapped in both singlet and triplet states:

$$\frac{\partial N_i(x, t)}{\partial t} = \frac{\partial N_s(x, t)}{\partial t} + \frac{\partial N_t(x, t)}{\partial t} \tag{7}$$

N_s and N_t denote the carrier population in singlet and triplet states, respectively. An energy-level relation between singlet and triplet states has been proposed [54]

$$N_s(x, t) = R_{st}e^{-\frac{\Delta E}{k_B T}}N_t(x, t) \tag{8}$$

where ΔE is the energy difference between the two split energy levels, and R_{st} is an energy-level degeneracy constant equal to 1/3. To simplify the notation, let

$$A(T) = R_{st}e^{-\frac{\Delta E}{k_B T}} \tag{9}$$

Furthermore, for the harmonic laser excitation at frequency $fre = \omega/2\pi$, $N_i(x, t)$, $n_T(x, t)$ and $G_0(x, t; \omega)$ can be written as,

$$N_i(x, t) = \frac{1}{2}N_i(x; \omega)(1+e^{i\omega t}) \tag{10a}$$

$$n_T(x, t) = \frac{1}{2}n_T(x; \omega)(1+e^{i\omega t}) \tag{10b}$$

$$G_0(x, t) = \frac{1}{2}G_0(x; \omega)\beta e^{-\beta x}(1+e^{i\omega t}) \tag{10c}$$

where ω is the modulation angular frequency and β is the optical absorption coefficient.

The kinetics of the trapping rate Eq. (5) can be modified in the frequency domain to yield an expression for the trapped carrier density $n_T(x; \omega)$

$$n_T(x; \omega) \approx \left(\frac{C_i N_T \tau_i}{1+i\omega\tau_i} \right) N_i(x, \omega) \tag{11}$$

where τ_i is defined by the carrier emission rate

$$\frac{1}{\tau_i(T)} = e_i(T) \tag{12}$$

Solving Eqs. (6)–(9) subject to frequency domain Eqs. (10), and taking only the modulated components gives

$$\frac{d^2 N_i(x, \omega)}{dx^2} - \frac{1}{D_h(T)}\left[i\omega + \frac{1}{\tau_E(T)} - \frac{R_T}{[1+A(T)][1+i\omega\tau_i(T; x, \omega)]} \right]N_i(x, \omega)$$
$$= -\frac{G_0\beta e^{-\beta x}}{D_h(T)[1+A(T)]} \tag{13}$$

Here, $\tau_E(T)$ is the effective carrier lifetime, defined as

$$\frac{1}{\tau_E(T)} \equiv \frac{1}{1+A(T)}\left[\frac{1}{\tau_i(T)} + \frac{A(T)}{\tau_s(T)} \right] \tag{14}$$

and $\tau_t(\tau_s)$ is the triplet (singlet) lifetime.

For CQD thin films with a thickness d (200 nm for CQD solar cell devices [18,34]), charge carriers at the boundaries should be quenched due to the high density of trap states. Eq. (13), therefore, can be solved with the boundary conditions: $N_i(x, \omega)=0$; $x = 0, d$, viz.

$$N_t(x, \omega) = B_1(\omega, T)e^{K_1 x} - B_2(\omega, T)e^{-K_1 x} + \left[\frac{K_2(T, \beta)}{K_1^2(T, \omega) - \beta} \right]e^{-\beta x} \tag{15}$$

Where the parameters are defined as

$$K_1^2(T; \omega) = \frac{1}{D_h(T)}\left\{ i\omega + \frac{1}{\tau_E(T)} - \frac{R_T}{[1+A(T)][1+i\omega\tau_i(T)]} \right\} \tag{16a}$$

$$K_2(T, \beta) = \frac{G_0\beta}{D_h(T)[1+A(T)]} \tag{16b}$$

$$B_1(\omega, T) = \left[\frac{K_2(T, \beta)}{K_1^2(T, \omega) - \beta^2} \right]\left(\frac{e^{-K_1 d} - e^{-\beta d}}{e^{K_1 d} - e^{-K_1 d}} \right) \tag{16c}$$

$$B_2(\omega, T) = \left[\frac{K_2(T, \beta)}{K_1^2(T, \omega) - \beta^2} \right]\left(\frac{e^{K_1 d} - e^{-\beta d}}{e^{K_1 d} - e^{-K_1 d}} \right) \tag{16d}$$

The radiative emission (i.e., PCR) signal can be expressed as an integral of the charge carrier population over the thickness of the active layer [60]:

$$S(\omega) = F(\lambda_1, \lambda_2) \int_0^d N_i(x, \omega)dx \tag{17}$$

Here, $F(\lambda_1, \lambda_2)$ is an instrumentation coefficient which depends on the spectral emission bandwidth $[\lambda_1, \lambda_2]$ of the near-infrared detector. From Eqs. (16 and 17), the final expression for the PCR signal can be obtained

$$\frac{S(\omega)}{F(\lambda_1, \lambda_2)} = \left[\frac{K_2(T, \beta)}{\beta^2 - K_1^2(T, \omega)} \right]\left\{ \frac{(1+e^{-\beta d})(1-e^{-K_1 d})^2}{K_1(1-e^{-2K_1 d})} - \frac{1}{\beta}(1-e^{-\beta d}) \right\} \tag{18}$$

It should be noted that when the trap state density $N_T=0$,

$$K_1(T; \omega) = \sqrt{\frac{1+i\omega\tau_E(T)}{D_h(T)\tau_E(T)}} = \frac{1}{L_h(T; \omega)} \tag{19}$$
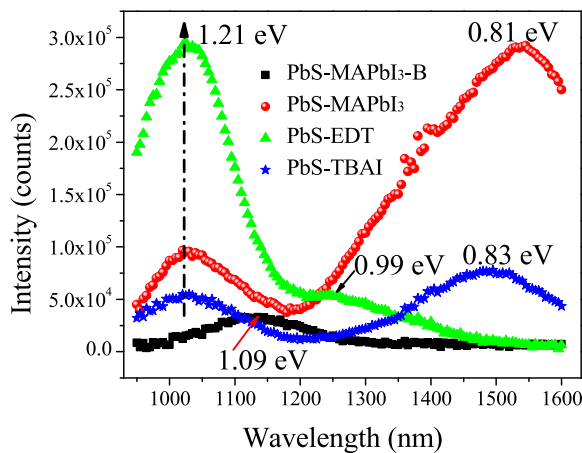
Fig. 2. Photoluminescence (PL) spectra of four PbS CQD thin films surface passivated with MAPbI$_3$, EDT, and TBAI.

which is the conventional carrier diffusion wavenumber [27], and $L_h(T;\omega)$ is the effective charge carrier hopping diffusion length.

3. Experimental methods

The PbS CQDs were synthesized and purified using a hot-injection approach and anti-solvent method, respectively [61]. CQDs were surface passivated with three different ligands: tetrabutylammonium iodide (TBAI), 1, 2-ethanedithiol (EDT), and methylammonium lead triiodide perovskite (MAPbI$_3$). The experimental surface passivation processes followed our previous reports [34,61]. These CQD thin films have a thickness of 200 nm as characterized by scanning electron spectroscopy. As shown in the room temperature PL spectra, Fig. 2, three CQD thin film samples capped with the abovementioned three ligands have the same band-to-band energy gap of 1.21 eV, while, for further investigation, perovskite MAPbI$_3$ was also applied to passivate CQD thin films with larger QD size, implying a smaller energy band gap of 1.09 eV. To clarify, the perovskite MAPbI$_3$ passivated PbS CQD thin film with larger dot size is labeled PbS-MAPbI$_3$-B throughout this paper, while the one with smaller dot size is labeled PbS-MAPbI$_3$. It is also shown in Fig. 2 that the PL peaks for each type of CQD thin films depend on the QD size, as well as on surface capping ligands. In addition, secondary PL emission peaks are also characterized, such as those at 0.81 eV (PbS-MAPbI$_3$) and 0.83 eV (PbS-TBAI), as well as the PL shoulder at 0.99 eV (PbS-EDT). These secondary PL emission peaks originate from recombiantions that occur through defect-induced donors/acceptors arising from unpassivated surface states, structural defects, or other changes induced during ligand exchange processes. Similar types of defect-induced donor/acceptor radiative emission have also been reported in other materials, such as ZnO nanowires [62], MoS$_2$ [63], and InP [64].

PCR frequency scans were also performed according to refs. [27,28]. Fig. 3 shows the experimental PCR setup for CQD thin films. A 1000 nm optical long-pass filter was placed in front of the InGaAs photodetector for the purpose of blocking the excitation beam, while due to the negligible thermal infrared contributions to the PCR signal, no short-pass filter was used. Based on its spectral bandwidth, the PCR detector collects PL emissions in a wavelength range between 1000 nm and 1700 nm. The sinusoidal excitation of an 830-nm laser was generated using a function generator to modulate the beam from 10 Hz to 100 kHz. Constant characterization temperatures in a range from 100 K to 300 K were maintained using a Linkam LTS350 cryogenic chamber. Photo-thermal spectroscopy was performed with the same PCR system at a fixed laser modulation frequency and scanning temperature. CQD thin films are promising candidates for QD photovoltaic devices; however, their efficiency is considerably
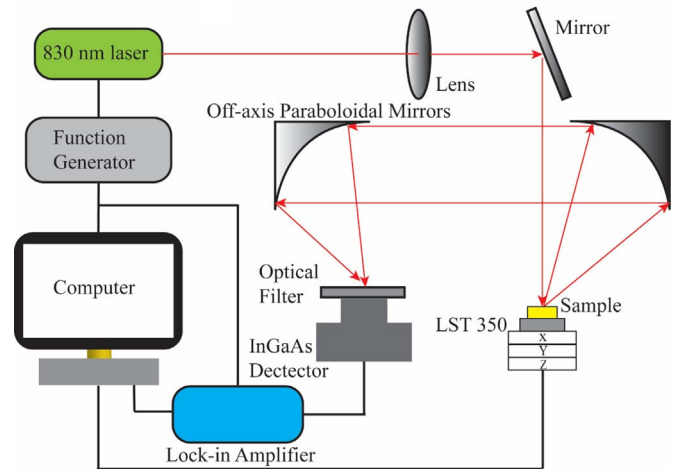

Fig. 3. Experimental setup for PCR frequency scans and photo-thermal spectroscopy temperature scans.

limited by mechanical and electrical defects in CQD thin film materials. Therefore, we performed homogeneity examination through homodyne lock-in carrierography imaging [50], as shown in Fig. 4. The image contrast arises from the modulated carrier wave (including free charge carriers and excitons) density distribution. Regions with high amplitude values originate from high carrier density, consistent with high carrier transport parameters including carrier lifetime, diffusivity, and low trap state density.

4. Results and discussion

4.1. Temperature-dependent transport kinetics

PCR can generate independent carrier diffusion-wave amplitude and phase channels simultaneously from a single frequency scan, both of which can be used for data analysis through best fitting in order to increase the accuracy and reliability of the best-fitted parameters. Detailed derivation of PCR amplitude and phase and the Matlab-based computational fitting for parameter extraction are discussed in the Supplementary information. Furthermore, a parametric theory as discussed in the Supplementary information is used to examine the uniqueness and reliability of the best-fitted parameters, and demonstrates that all six parameters can be resolved in the framework of our equations and experimental data sets. For example, Fig. S1 shows the determinants and sensitivity coefficients for parameters D_h and τ_E. Therefore, this validated methodology was employed for parameter extraction through this study. The experimental and best-fitted PCR amplitude and phase frequency scans of PbS-MAPbI$_3$ at various temperatures (300–100 K), using Eq. (18), (S1) and (S2), are presented in Fig. 5. Due to the reduced carrier-phonon interactions at low temperatures and a concomitant increase in the radiative emission rate accomplished by a decrease in the nonradiative decay rate, the PCR amplitude increases at low temperatures. In addition, at low temperatures, the increased carrier lifetime yields an increased PCR phase lag when compared with that at higher temperatures.

Fig. 6(a), (c)–(f) and Table 1 show the measurements of five temperature-dependent carrier hopping transport parameters: D_h, τ_E, R_T, e_i, and L_h of PbS-MAPbI$_3$. With the increase in temperature from 100 K to 300 K, the best-fitted hopping diffusivity D_h increases dramatically from 1.04×10^{-6} cm^2/s to 2.41×10^{-3} cm^2/s. The latter value is comparable to the previously reported values of 0.012 cm^2/s and 0.003 cm^2/s [29] measured at room temperature by transient PL spectroscopy for 3-mercaptopropionic acid (MPA) and 8-mercaptooc-tanoic acid (MOA) passivated CQD thin films, respectively. The temperature-dependent behavior of the carrier-wave diffusivity D_h is
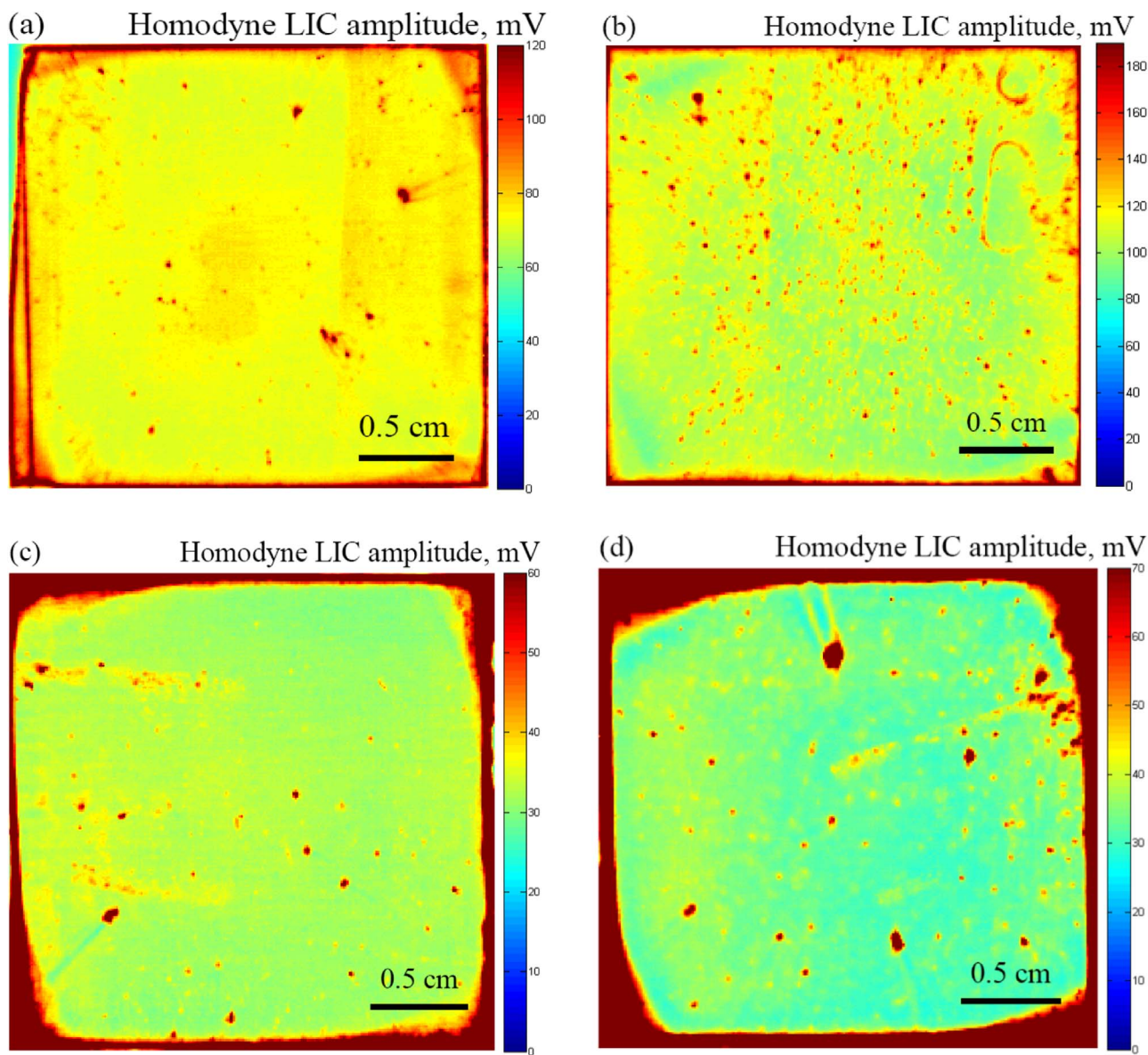
Fig. 4. Homodyne lock-in carrierography images of PbS-MAPbI$_3$ (a), PbS-MAPbI$_3$-B (b), PbS-EDT (c), and PbS-TBAI (d) measured at 10 Hz. Note all the samples were placed on an aluminum platform for imaging.

consistent with the phonon-assisted carrier hopping transport mechanism. It should be noted that a tunneling transport mechanism is not taken into consideration due to its non-phonon-assisted transport nature [21,24,65–68]. Hopping transport of carriers within the CQD assembly is carried out through the temperature-dependent nearest neighbor hopping (NNH) or Efros-Shklovskii variable-range-hopping (ES-VRH) [21,23,25,33]. NNH does not occur at extremely low temperatures because, on average, hopping between nearest neighbor states requires higher activation energy [25]. Hopping distance is always optimized spontaneously to yield the highest carrier mobility, and the optimized distance decreases with increasing temperature [25,69]. With the temperature rising above a threshold value, carrier hopping behavior switches from ES-VRH to NNH which has the same hopping distance as the interdot spacing determined by thermal energy. Kang et al. [25] found that the hopping distance was longer than the interdot spacing at lower temperatures, and the optimized distance was equal to the nearest neighbor distance in a temperature range from 40 K to 75 K, indicating a threshold temperature lower than the minimum temperature of this study. Eq. (4), which does not assume a conventional Einstein relation, predicts an exponential

increase in D_h with increasing temperature, and an exponential decrease with increasing average barrier width (ligand length). Furthermore, Fig. 6(b) shows the activation energy (96.2 meV) obtained from the Arrhenius plot of the trap-state-mediated hopping diffusivity. It should be reiterated that the calculated activation energy is trap-state-mediated, i.e., an average energy barrier must be overcome when carriers hop over the interdot energy barrier and hop out of trap states, as shown in Fig. 1(b). The activation energy extracted from the D_h Arrhenius plot is consistent with those obtained from the thermal emission rate e_i as well as those from the photo-thermal spectra which will be discussed later, corresponding to shallow trap states with an energy depth much smaller than that of defect-related states measured by PL (Fig. 2). These activation energy values are mirrored by the shallow trap states of *ca*. 0.1 eV (from the conduction band) obtained from photocurrent quenching [70,71].

Fig. 6(c) shows the same trends of carrier lifetime dependence on temperature as our earlier reported results [27,28]: carrier lifetime increases with decreasing temperature which is due to the reduced non-radiative decay rate at low temperatures, a result of decreased phonon-carrier interactions. Similar values of carrier lifetimes at room
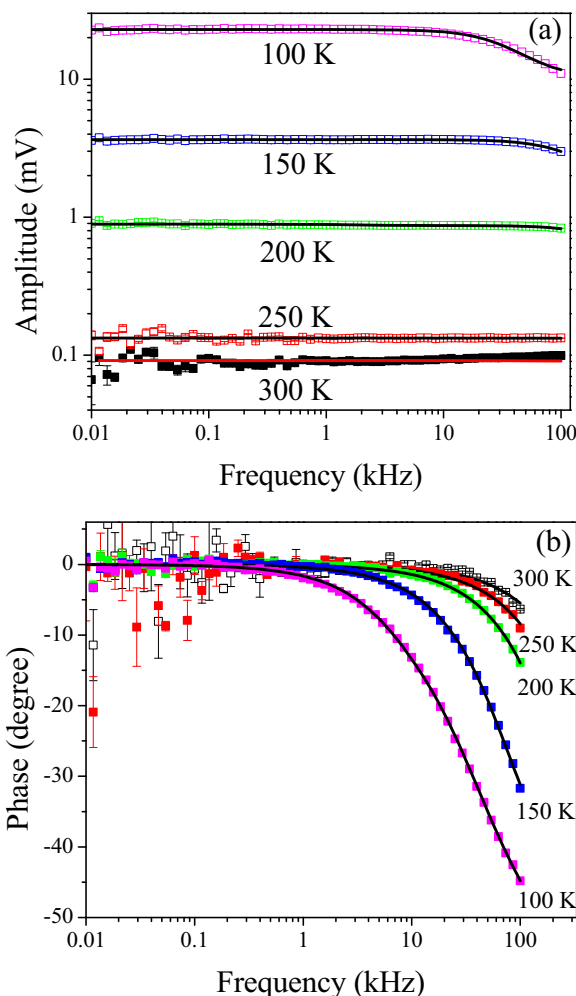
Fig. 5. PCR amplitude (a) and phase (b) of MAPbI$_3$-passivated CQD thin films (PbS-MAPbI$_3$) measured at various frequencies ranging from 10 Hz to 100 kHz and temperatures between 100 K and 300 K.

temperature can also be found elsewhere [27,28,72–75] in a range from 0.01 μs to 5 μs. Carrier lifetime can be influenced by many intrinsic QD properties including size, surface ligands, and QD composition. Fig. 6(d) and (e) show the temperature-dependent carrier trapping rate R_T and the thermal emission rate e_i, respectively. Table 1 shows that e_i increases from ~10^4 s^{-1} at 100 K to ~10^8 s^{-1} at 300 K. The activation energy of 106.3 meV, originating from shallow trap states, were extracted from the Arrhenius plot of e_i as shown in Fig. 6(e) and is in agreement with the activation energy measured from the hopping diffusivity D_h. At lower temperatures, more carriers are localized at the excitation sites and the smaller population of phonons freezes these photogenerated carriers in trap states, which is mirrored by the much lower hopping diffusivity D_h when compared with the values obtained at room temperature. Therefore, it is reasonable to conclude that, with the help of phonons at high temperatures, the more widely distributed carriers are subject to a relatively higher carrier trapping rate, i.e., at high temperature more trap states are empty which results in an increased R_T. Furthermore, due to the higher ambient thermal energy, the thermal emission rate from the trap states is higher as shown in Fig. 6(e). Using the best-fitted D_h and τ_E values, the hopping diffusion lengths were calculated through $L_h = (\tau_E D_h)^{1/2}$, Fig. 6(f). Although τ_E decreases with temperature, the hopping diffusion length still increases dramatically from 23 nm to 0.33 μm when the temperature rises from 100 K to 300 K, because the diffusivity increase is stronger than the lifetime decrease. Diffusion length is capping-ligand-dependent, for example, at room temperature, diffu-

sion lengths of PbS CQD thin films treated with different ligands vary widely: with partially fused PbS CQDs (230 nm) [76], with CdCl$_2$ (80 nm) [43], with ethanethiol (140 nm) [77], and with 3-mercapto-propionic acid (MPA, 100–1000 nm) [78]. Notwithstanding the fact that the hopping diffusion length can vary as a function of probe method, the D_h values at room temperature obtained in this study additionally indicate the high photocarrier diffusion ability of the perovskite photovoltaic material MAPbI$_3$.

Fig. 7 shows the Arrhenius plots of the temperature-dependent PCR amplitude at temperatures ranging from 90 K to 300 K. Taking into the consideration of both radiative and non-radiative recombination pathways in PbS CQD thin films, the temperature-dependent dynamic PL (PCR amplitude) intensity $I(T)$ can be described by the following expression [79–81]

$$I(T) = \frac{I_0}{1 + \sum_i A_i exp\left(-\frac{E_i}{k_B T}\right)}$$

(20)

where I_0 is a normalizing factor, E_i is the activation energy of the process (i), and A_i is the carrier transition rate for process (i). The activation energy is the energy difference between the original and the final energy states within a carrier transition process. Here, we assume that our exciton complexes are in the ground state with energy E_O and at least two carrier transition channels with higher energy states E_1 and E_2, which have to be overcome for the transition process of excitons to occur. It should be noted that the distribution of excitons in these three levels is govern by Boltzmann statistics featuring an equilibrium temperature behavior [79], which leads to the derivation of Eq. (20) with i=2. Therefore, the activation energy can be expressed as: $E_{a,1}=E_1-E_O$ and $E_{a,2}=E_2-E_O$. The PL emission of PbS CQD thin films in the entire experimental temperature range cannot be fitted using only one activation energy level as different carrier dynamic transport processes dominate in different temperature ranges. The best-fitted curves to the photo-thermal spectra of the four samples using Eq. (20), Fig. 7, are the results of two strategies applied for the fitting: first, the entire thermal spectrum was fitted across the entire temperature range, while the number of activation energy levels was increased until a satisfactory fit was achieved. For PbS-EDT, PbS-MAPbI$_3$, and PbS-MAPbI$_3$-B, two activation levels were found to be adequate. When three levels were attempted for these samples, the third activation energy was identical to one of the first two activation energies. Compared with other samples, PbS-TBAI exhibits two distinguishable trends in the entire temperature range, which cannot be accounted for by Eq. (20). Therefore, the PbS-TBAI data were split into two regimes using the dashed line boundary in Fig. 7. The two sub-ranges were fitted separately, using two energy levels (high tempera-ture end) and one energy level (low temperature end). Second, to investigate the temperature-dependent trap effects on carrier trans-port, each spectrum was divided into 5 parts with 100 K, 150 K, 200 K, 250 K, and 300 K being the average temperature (central temperature) in each range, and then each range was fitted using only one energy level through Eq. (20). All the best-fitted activation energies through these two strategies are summarized in Table 2.

Generally, a higher activation energy, accounting for the trap-state-related thermally activated carrier transition process, dominates in the high-temperature range. In comparison, at relatively low temperatures, lower activation energies are usually observed, which can be ascribed to phonon energy [82], exciton binding energy [82–85], and exciton dislocation binding energy [84]. As shown in Table 2, thermal quenching was observed across the entire temperature range and the activation energy increases with temperature for all samples. The temperature-dependent activation energy of PbS CQD thin films using the same method was also reported by Wang et al. [51]. Therefore, as shown in Fig. 1(b), $E_{a,2}$ is associated with shallow trap states, and the best-fitted values are close to the activation energies measured from the
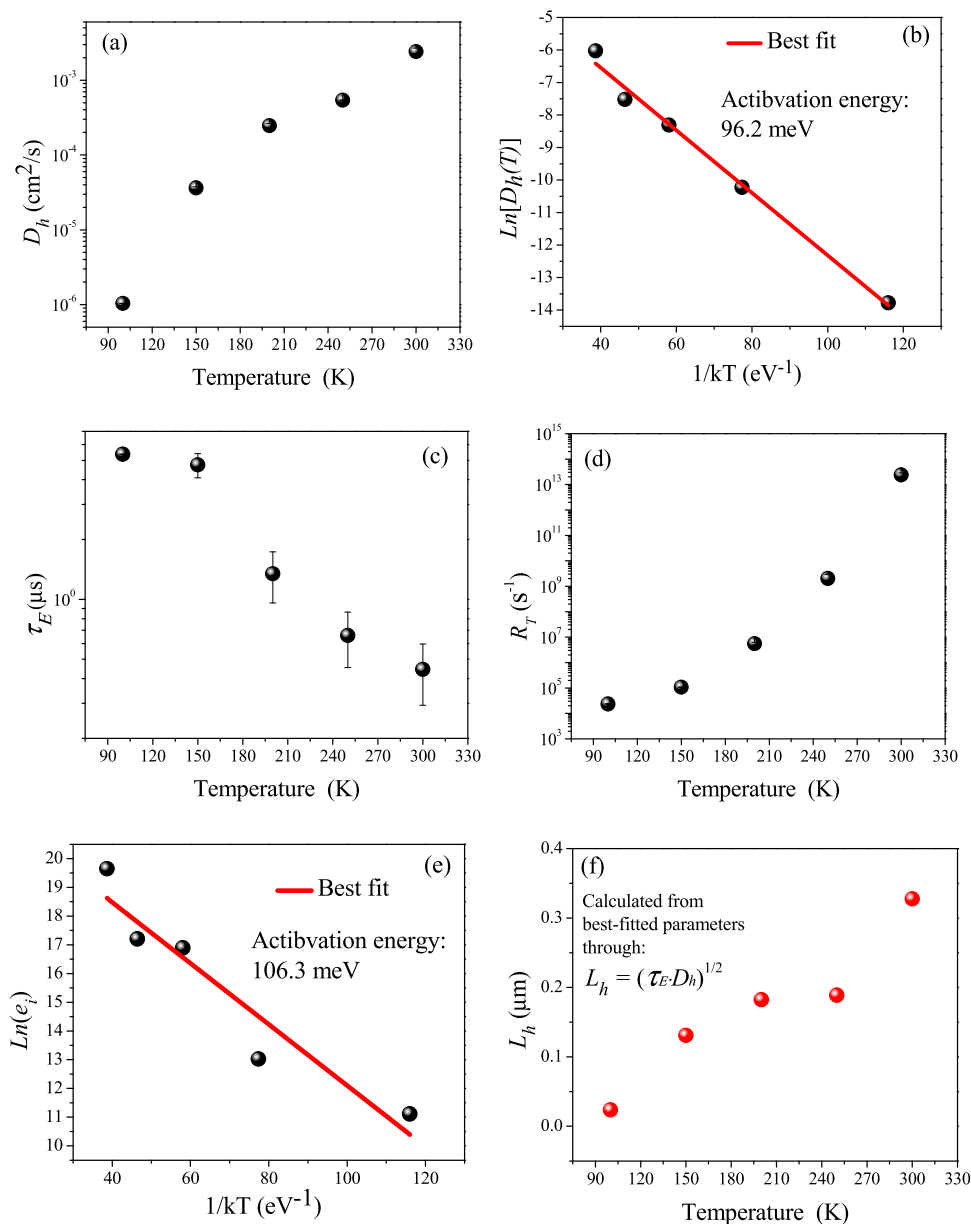
Fig. 6. Best-fitted hopping diffusivity D_h (a), and Arrhenius plot of D_h for the extraction of the carrier hopping transport activation energy (b) of the MAPbI$_3$-passivated (PbS-MAPbI$_3$) CQD thin film. For the same sample, (c)-(e) are the best-fitted effective exciton lifetime τ_E, carrier trapping rate R_T, and Arrhenius plot of thermal emission rate e_i, respectively. (f) Carrier hopping diffusion length L_h calculated from the best-fitted τ_E and D_h values.

carrier hopping diffusivity [Fig. 6(b)], and from the thermal emission rate [Fig. 6(e)]. As shown in Fig. 1(b), contrary to deep level trap states, which operate as recombination centers, carriers that are trapped in these shallow trap states do not recombine but escape from these traps quickly. Nevertheless, it is difficult to identify the source of $E_{a,1}$ based

on this study. In Table 2, with the exception of PbS-TBAI, activation energies E_a at 300 K are higher than either $E_{a,1}$ or $E_{a,2}$. Moreover, E_a at 100 K is almost equal to $E_{a,1}$ (except for PbS-MAPbI$_3$-B with bigger dot size), which is consistent with the elimination of shallow-trap-state-related carrier transport processes as contributors to the activation

Table 1
Best-fitted parameters for PbS-MAPbI$_3$ CQD thin films at different temperatures.

| Parameters	Temperature (K)				
	300	250	200	150	100
Hopping diffusivity D_h (cm^2/s)	$2.41\times10^{-3} \pm 2.75\times10^{-4}$	$5.41\times10^{-4} \pm 1.76\times10^{-6}$	$2.47\times10^{-4} \pm 1.72\times10^{-5}$	$3.62\times10^{-5} \pm 1.44\times10^{-6}$	$1.04\times10^{-6} \pm 3.93\times10^{-13}$
Effective carrier lifetime τ_E (µs)	0.45 ± 0.15	0.66 ± 0.21	1.35 ± 0.39	4.75 ± 0.65	$5.37 \pm 3.68\times10^{-8}$
Trapping rate R_T (s^{-1})	$2.40\times10^{13} \pm 4.55\times10^{12}$	$2.02\times10^{9} \pm 2.37\times10^{8}$	$5.54\times10^{6} \pm 6.93\times10^{5}$	$1.08\times10^{5} \pm 3.70\times10^{2}$	$2.36\times10^{4} \pm 8.99\times10^{-4}$
Thermal emission rate e_i (s^{-1})	$3.41\times10^{8} \pm 1.22\times10^{8}$	$2.97\times10^{7} \pm 9.38\times10^{6}$	$2.18\times10^{7} \pm 3.45\times10^{5}$	$4.55\times10^{5} \pm 5.33\times10^{2}$	$6.70\times10^{4} \pm 0.00059$
Hopping diffusion length L_h (µm)	0.33	0.19	0.18	0.13	0.023
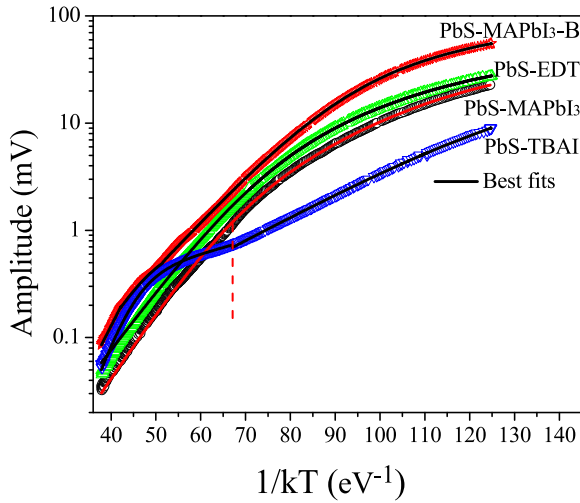
Fig. 7. Temperature scans of the PCR amplitude for different ligands passivated PbS CQD thin films. The continuous lines are the best fits to each set of data using Eq. (20).

energy $E_{a,2}$. Nonetheless, the $E_{a,1}$ process is active throughout the entire temperature range regardless of the type of surface capping ligands and QD size. Also, the value of $E_{a,1}$ is consistent with the exciton binding energy in a range from 50 to 200 meV for QDs with a diameter of 1–2 nm [86]. In addition, the exciton dissociation occurs in the course of all carrier transport kinetics in our experimental temperature range. Therefore, it is reasonable to assign $E_{a,1}$ to be the exciton binding energy (E_b) as depicted in Fig. 1(b). It should also be noted from Fig. 1(b) that the exciton binding energy in quantum confined systems is the energy difference between exciton transition (optical gap, $E_{g,opt}$) and electronic bandgap (E_g), i.e., $E_b = E_g - E_{g,opt}$, which can be approximated through the electron-hole Coulomb interaction [86] and affected by the material dielectric constant. Electron-hole Coulomb interaction predicts that exciton binding energy is proportional to $1/R$ [86], where R is the radius of the QDs. This is consistent with the much smaller $E_{a,1}$ (i.e. E_b, 35.21 meV) of PbS-MAPbI$_3$-B than that of other CQD thin films, as exciton binding energies for smaller CQDs (PbS-EDT, PbS-TBAI, and PbS- MAPbI$_3$) have higher values ranging from 45.21 meV to 53.20 meV. This measured exciton binding energy is similar to the activation energy of *ca.* 40 meV for exciton dissociation in the PbS CQD solar cell as reported by Gao et al. [30] and in PbSe QD films measured by Mentzel et al. [11]. As for PbS-TBAI, the activation energy does not exhibit a monotonic increase with temperature. The additional activation energy $E_{a,3}$ of 25.91 meV might result from many possible mechanisms, such as exciton delocalization energy [84] from donors or acceptors resulting from the capping ligand TBAI. The identification of $E_{a,3}$ needs further investigation.

The foregoing discussion summarizes that activation energies E_a for CQD thin films arise from two carrier transition channels except that for PbS-TBAI which has three channels, i.e. exciton dissociation

($E_{a,1}$) and shallow-trap-related thermal activation ($E_{a,2}$). Consequently, the extraction of E_a using Eq. (20) at only one activation energy level is subject to the assumption that, in each temperature range (with a central temperature of 300 K, 250 K, 200 K, 150 K, or 100 K), only one carrier transition process ($E_{a,1}$ or $E_{a,2}$) is dominant. It should be noted that deeper lying trap states require higher E_a for carrier transitions, as expected. Therefore, comparing E_a values at different central temperatures (Table 2) with the corresponding $E_{a,1}$ and $E_{a,2}$ as discussed above, it must be kept in mind that the exciton dissociation process occurs across the entire temperature range, while the activation energies ($E_{a,2}$) for trap-mediated carrier transitions decrease with decreasing temperature. Furthermore, at the low temperature of 100 K, E_a for all samples is approximately equal to $E_{a,1}$, indicating a negligible contribution of $E_{a,2}$ to the overall activation energy at this temperature. All of these facts point to the following conclusion: deep-lying trap states dominate carrier transport at higher temperatures, while shallow trap states control carrier transport at low temperatures, in agreement with [51]. These effects may arise because carrier distributions are localized near their generation sites at low temperatures due to the low values of D_h.

4.2. Ligand-dependent transport kinetics

Eq. (18) describes the PCR signals generated by the carrier transport in CQD thin films. Besides temperature, surface passivation ligands and the QDs geometry are also substantial factors to carrier transport properties in CQD thin films [21,23–26,31,33]. In addition to passivating QD unsaturated surface bonds to minimize or eliminate surface trap states, solution exchange ligands reduce the interdot spacing and enhance the coupling strength between neighboring QDs. When trap states are not the dominant factors for carrier hopping transport, smaller interdot spacing, according to Eq. (4), results in increased diffusivity. Fig. 8 shows the PCR amplitude and phase frequency scans at 100 K for CQD thin films passivated with four different ligands and the best fits of Eq. (18) to each curve. The best-fitted parameters of carrier transport properties in these CQD thin films are tabulated in Table 3. The interdot spacing values of PbS-TBAI and PbS-MAPbI$_3$ CQD thin films measured by grazing-incidence small-angle scattering (GISAXS) are 3.50 nm and 3.30 nm, respectively [87]. In addition, Liu et al. [24] calculated the nominal EDT length to be ca. 0.43 nm which should result in a smaller interdot spacing than the other ligands due to its smaller molecule size. The small interdot spacing of PbS-EDT allows the increase of hopping diffusivity above that of MAPbI$_3$ passivated CQD thin films, consistent with Eq. (4). The slightly higher carrier diffusivity of PbS-MAPbI$_3$ than PbS-MAPbI$_3$-B originates in the lower hopping activation energy of PbS-MAPbI$_3$ (59.55 meV) at 100 K than PbS-MAPbI$_3$-B (69.96 meV) with shallow, yet deeper lying, trap states, as shown in Table 2. On the contrary, at 300 K, when trap states start to play key roles in carrier hopping transport, PbS-MAPbI$_3$ carriers face higher transport activation energy (275.90 meV) than PbS-MAPbI$_3$-B carriers (190.94 meV), Table 2, resulting in a smaller D_h (2.41×10^{-3} cm^2/s) than PbS-MAPbI$_3$-B

Table 2
Activation energies at different temperatures for PbS CQD thin films passivated with various ligands.

| Samples	Activation energy fitted in separate temperature range (one level fitting) (meV)					Activation energy fitted across the whole temperature range (meV)		
	E_a					$E_{a,1}$	$E_{a,2}$	$E_{a,3}$
	300 K	250 K	200 K	150 K	100 K			
PbS-MAPbI$_3$	275.90	147.51	110.87	98.77	59.55	53.20	147.41	
PbS-MAPbI$_3$-B	190.94	170.23	92.25	95.98	69.96	35.21	107.24	
PbS-TBAI	233.81	236.27	77.92	46.45	52.25	51.55	273.94	25.91
PbS-EDT	172.94	148.36	113.63	101.29	59.35	45.21	129.94	
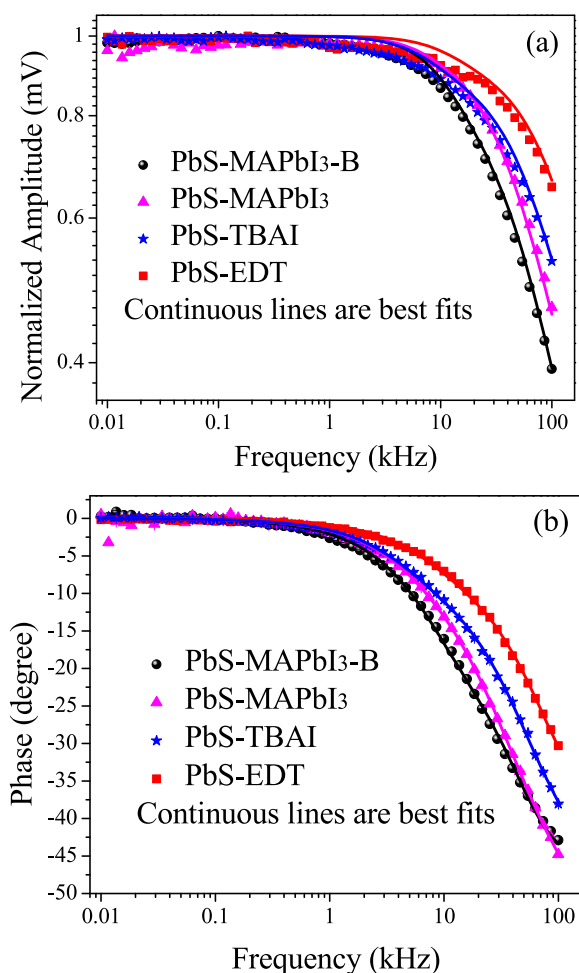
Fig. 8. 100 K PCR amplitudes (a) and phases (b) of CQD thin films passivated with four different ligands, and the best fits to each curve using Eq. (18).

$(1.80 \times 10^{-2}$ cm^2/s), Table 4. In addition, the values of activation energies obtained from the photo-thermal spectra also explain the slightly higher D_h of PbS-TBAI (E_a=233.81 meV) than that of PbS-MAPbI$_3$ CQD thin films, as both samples feature significant defect-related states, Fig. 2, which seem to become limiting factors of the carrier hopping diffusion at room temperature. Unfortunately, the PCR signal resolution (i.e., phase lag and amplitude decrease) for the PbS-EDT samples is too low to be resolved and fitted for the extraction of these parameters even when the modulation frequency is increased to 1 MHz. This is not a limitation inherent in the PCR technique, but rather a consequence of the inability of our equipment to measure samples with too poor transport properties.

The effective carrier lifetime ,τ_E, and the thermal emission rate, e_i, at 100 K, are summarized for all ligands in Table 3. Consistently with

the foregoing mechanism of the temperature-dependent carrier hopping lifetime as shown in Table 1, values of τ_E for PbS-TBAI (0.16 μs) and PbS- MAPbI$_3$-B (0.51 μs) at 300 K greatly increase when the temperature decreases to 100 K (3.79 μs and 7.66 μs, respectively) as shown in Table 3. On the contrary, the thermal emission rate e_i was found to significantly increase from ~10^4 s^{-1} at 100 K (Table 3) for all samples to ~10^{10} s^{-1} at 300 K (Table 4). Comparing all three samples, PbS-MAPbI$_3$-B at 300 K exhibits the highest thermal emission rate e_i. Returning to the effective carrier lifetime τ_E, MAPbI$_3$-passivated PbS CQD thin films exhibit longer lifetime at 100 K than PbS-EDT and PbS-TBAI, while PbS-MAPbI$_3$-B lifetime remains the highest amongst all the tested samples at both 100 K (Table 3) and 300 K (Table 4). This is not unexpected because PbS-MAPbI$_3$-B does not exhibit any defect states induced secondary PL emission peak as shown in Fig. 2.

Regarding the calculated diffusion length L_h, both MAPbI$_3$-passivated samples have similar L_h of *ca.* 24–26 nm at 100 K, a temperature at which the influence of trap states is not significant. These values are higher than those of TBAI and EDT treated samples, Table 3. Considering the QD size (~2 nm) and interdot spacing (~3 nm), the short diffusion length indicates that carriers hop across only a few QDs before statistically recombining. At 300 K, trap states limit carrier transport which is, nevertheless, assisted by phonon interactions in overcoming the hopping activation energy. This trade-off between trap-state limitations and phonon assistance results in longer diffusion lengths L_h at high temperature. Tables 3 and 4 show that PbS-MAPbI$_3$-B possesses the longest L_h at both high and low temperatures, indicating that this material is optimal for solar cell performance improvement.

The carrier trapping rate R_T as defined in Section 2 is proportional to the trap state density and was measured to be on the order of 10^4 s^{-1} at 100 K (Table 3). Consistently with the PL spectra in Fig. 2, PbS-MAPbI$_3$, as shown in Table 3, was fitted with higher R_T than PbS-MAPbI$_3$-B. In addition, the strong trap peak of the PbS-TBAI spectrum is also consistent with its higher R_T than that of PbS-EDT. MAPbI$_3$-capped PbS CQD thin films exhibit relatively lower carrier trapping rates than PbS-EDT and PbS-TBAI (Table 3) due to the smaller lattice mismatch between PbS and the MAPbI$_3$ perovskite material [49] which results in better surface passivation. The absorption coefficient β at 100 K (Table 3), is on the order of 10^6 cm^{-1} for all samples except PbS-EDT with a slightly higher value of 8.57×10^7 ($\pm 2.83 \times 10^6$). From the same table, the exciton generation rate G_O at 100 K is between 3×10^7 cm^{-3} s^{-1} and 2×10^9 cm^{-3} s^{-1} for all our PbS CQD thin films.

5. Conclusions

We developed a novel quantitative methodology to characterize carrier transport dynamics for QD systems by using the fully optical non-destructive PCR technique and by deriving a trap-state-mediated carrier hopping transport model. Multiple materials and carrier transport parameters for PbS-EDT, PbS-TBAI, PbS-MAPbI$_3$, and PbS-MAPbI$_3$-B CQD thin films were measured at different temperatures. The observed monotonic dependence of effective carrier lifetime τ_E,

Table 3
Summary of the best-fitted parameters for CQD thin films surface passivated with various ligands. These parameters were evaluated for 100 K measurement.

Samples	PbS-EDT	PbS-TBAI	PbS-MAPbI$_3$-B	PbS-MAPbI$_3$
Hopping diffusivity D_h (cm^2/s)	$1.62 \times 10^{-6} \pm 2.83 \times 10^{-8}$	$8.58 \times 10^{-7} \pm 3.74 \times 10^{-13}$	$8.82 \times 10^{-7} \pm 6.07 \times 10^{-14}$	$1.04 \times 10^{-6} \pm 3.93 \times 10^{-13}$
Effective carrier lifetime τ_E (μs)	$2.78 \pm 7.13 \times 10^{-6}$	$3.79 \pm 1.42 \times 10^{-8}$	$7.66 \pm 3.53 \times 10^{-8}$	$5.37 \pm 3.68 \times 10^{-8}$
Thermal emission rate e_i (s^{-1})	$6.53 \times 10^4 \pm 1.16$	$6.80 \times 10^4 \pm 0.00086$	$4.96 \times 10^4 \pm 0.0010$	$6.70 \times 10^4 \pm 0.00059$
Trapping rate R_T (s^{-1})	$4.72 \times 10^4 \pm 0.80$	$5.24 \times 10^4 \pm 3.71 \times 10^{-4}$	$2.04 \times 10^4 \pm 3.43 \times 10^{-4}$	$2.36 \times 10^4 \pm 8.99 \times 10^{-4}$
Absorption coefficient β (cm^{-1})	$8.57 \times 10^7 \pm 2.83 \times 10^6$	$6.22 \times 10^6 \pm 1.43$	$7.80 \times 10^6 \pm 0.34$	$2.79 \times 10^6 \pm 0.56$
Generation rate G_O (cm^{-3} s^{-1})	$1.84 \times 10^9 \pm 7.22 \times 10^7$	$1.81 \times 10^8 \pm 3.12$	$1.44 \times 10^8 \pm 2.50$	$3.04 \times 10^7 \pm 0.31$
Diffusion length L_h (μm)	0.017	0.018	0.026	0.024
Interdot spacing (nm)	0.43 (nominal ligand length) [24]	3.50 [87]	3.30 [87]	3.30 [87]

Table 4

Summary of the best-fitted parameters for CQD thin films surface passivated with various ligands. These parameters were evaluated for 300 K measurement.

Samples	PbS-TBAI	PbS-MAPbI$_3$-B	PbS-MAPbI$_3$
Hopping diffusivity D_h (cm^2/s)	$5.09\times10^{-3} \pm 6.96\times10^{-4}$	$1.80\times10^{-2} \pm 2.30\times10^{-3}$	$2.41\times10^{-3} \pm 2.75\times10^{-4}$
Effective carrier lifetime τ_E (µs)	0.16 ± 0.06	0.51 ± 0.15	0.45 ± 0.15
Thermal emission rate e_i (s^{-1})	$7.35\times10^9 \pm 4.93\times10^9$	$8.33\times10^{10} \pm 5.78\times10^{10}$	$6.99\times10^9 \pm 1.35\times10^9$
Diffusion length L_h (µm)	0.29	0.96	0.33

hopping diffusivity D_h, carrier trapping rate R_T, and hopping diffusion length L_h on the temperature in the range from 100 K to 300 K is consistent with a phonon-assisted carrier hopping transport mechanism in PbS CQD thin films. For all samples, trap-state-mediated activation energies were found to be in a range between 100 meV and 280 meV. Photo-thermal spectroscopy was also used to measure exciton binding energies as a function of dot size. From PL spectroscopy, it was shown that perovskite (MAPbI$_3$) passivated thin films with larger dot size (bandgap energy: 1.09 eV) are free of obvious defect states induced secondary PL emission. These thin films exhibited the highest carrier lifetime and hopping diffusivity at 300 K, thus proving to be better photovoltaic materials than PbS-MAPbI$_3$, as well as TBAI, or EDT treated CQD thin films. The PCR technique generates new insights into the temperature- and ligand-dependent carrier transport dynamics in photovoltaic CQD thin films, hence, benefiting CQD solar cell efficiency optimization through a better understanding of device energy dissipation physics by means of quantitative recombination process analysis in CQD surface trap states with a goal to minimizing their effects through ligand passivation and bandgap energy engineering. The results of this study can be further applied in directing high-efficiency CQD solar cell fabrication in conjunction with the development of an improved PCR theory for photovoltaic devices.

Acknowledgements

Appendix A. Supporting information

Supplementary data associated with this article can be found in the online version at doi:10.1016/j.solmat.2017.02.024.

References

[1] B.L. Wehrenberg, C. Wang, P. Guyot-Sionnest, Interband and intraband optical studies of PbSe colloidal quantum dots, J. Phys. Chem. B 106 (41) (2002) 10634–10640.
[2] E.H. Sargent, Infrared quantum dots, Adv. Mater. 17 (5) (2005) 515–522.
[3] V. Sukhovatkin, S. Hinds, L. Brzozowski, E.H. Sargent, Colloidal quantum-dot photodetectors exploiting multiexciton generation, Science 324 (5934) (2009) 1542–1544.
[4] M.C. Beard, J.C. Johnson, J.M. Luther, A.J. Nozik, Multiple exciton generation in quantum dots versus singlet fission in molecular chromophores for solar photon conversion, Philos. Trans. R. Soc. Lond. A: Math. Phys. Eng. Sci. 373 (2044) (2015) 20140412.
[5] M.C. Beard, Multiple exciton generation in semiconductor quantum dots, J. Phys. Chem. Lett. 2 (11) (2011) 1282–1288.
[6] W.A. Tisdale, K.J. Williams, B.A. Timp, D.J. Norris, E.S. Aydil, X.Y. Zhu, Hot-electron transfer from semiconductor nanocrystals, Science 328 (5985) (2010) 1543–1547.
[7] B.L. Wehrenberg, P. Guyot-Sionnest, Electron and hole injection in PbSe quantum dot films, J. Am. Chem. Soc. 125 (26) (2003) 7806–7807.
[8] M.S. Kang, J. Lee, D.J. Norris, C.D. Frisbie, High carrier densities achieved at low voltages in ambipolar PbSe nanocrystal thin-film transistors, Nano Lett. 9 (11) (2009) 3848–3852.
[9] D.V. Talapin, C.B. Murray, PbSe nanocrystal solids for n-and p-channel thin film field-effect transistors, Science 310 (5745) (2005) 86–89.
[10] S.Z. Bisri, E. Degoli, N. Spallanzani, G. Krishnan, B.J. Kooi, C. Ghica, M. Yarema, W. Heiss, O. Pulci, S. Ossicini, M.A. Loi, Determination of the electronic energy levels of colloidal nanocrystals using field-effect transistors and ab-initio calculations, Adv. Mater. 26 (32) (2014) 5639–5645.
[11] T.S. Mentzel, V.J. Porter, S. Geyer, K. MacLean, M.G. Bawendi, M.A. Kastner, Charge transport in PbSe nanocrystal arrays, Phys. Rev. B 77 (7) (2008) 075316.
[12] J.P. Clifford, G. Konstantatos, K.W. Johnston, S. Hoogland, L. Levina, E.H. Sargent, Fast, sensitive and spectrally tuneable colloidal-quantum-dot photodetectors, Nat. Nanotechnol. 4 (1) (2009) 40–44.
[13] G. Konstantatos, I. Howard, A. Fischer, S. Hoogland, J. Clifford, E. Klem, L. Levina, E.H. Sargent, Ultrasensitive solution-cast quantum dot photodetectors, Nature 442 (7099) (2006) 180–183.
[14] G. Konstantatos, J. Clifford, L. Levina, E.H. Sargent, Sensitive solution-processed visible-wavelength photodetectors, Nat. Photonics 1 (9) (2007) 531–534.
[15] A.G. Pattantyus-Abraham, I.J. Kramer, A.R. Barkhouse, X. Wang, G. Konstantatos, R. Debnath, L. Levina, I. Raabe, M.K. Nazeeruddin, M. Gratzel, E.H. Sargent, Depleted-heterojunction colloidal quantum dot solar cells, ACS Nano 4 (6) (2010) 3374–3380.
[16] X. Wang, G.I. Koleilat, J. Tang, H. Liu, I.J. Kramer, R. Debnath, L. Brzozowski, D.A.R. Barkhouse, L. Levina, S. Hoogland, E.H. Sargent, Tandem colloidal quantum dot solar cells employing a graded recombination layer, Nat. Photonics 5 (8) (2011) 480–484.
[17] I.J. Kramer, E.H. Sargent, The architecture of colloidal quantum dot solar cells: materials to devices, Chem. Rev. 114 (1) (2013) 863–882.
[18] L. Hu, A. Mandelis, X. Lan, A. Melnikov, S. Hoogland, E.H. Sargent, Imbalanced charge carrier mobility and Schottky junction induced anomalous current-voltage characteristics of excitonic PbS colloidal quantum dot solar cells, Sol. Energ. Mater. Sol. C 155 (2016) 155–165.
[19] X. Gong, Z. Yang, G. Walters, R. Comin, Z. Ning, E. Beauregard, V. Adinolfi, O. Voznyy, E.H. Sargent, Highly efficient quantum dot near-infrared light-emitting diodes, Nat. Photonics 10 (2016) 253–257.
[20] Z. Yang, O. Voznyy, M. Liu, M. Yuan, A.H. Ip, O.S. Ahmed, L. Levina, S. Kinge, S. Hoogland, E.H. Sargent, All-quantum-dot infrared light-emitting diodes, ACS Nano 9 (12) (2015) 12327–12333.
[21] I.H. Chu, M. Radulaski, N. Vukmirovic, H.P. Cheng, L.W. Wang, Charge transport in a quantum dot supercrystal, J. Phys. Chem. C 115 (43) (2011) 21409–21415.
[22] H.E. Romero, M. Drndic, Coulomb blockade and hopping conduction in PbSe quantum dots, Phys. Rev. Lett. 95 (15) (2005) 156801.
[23] S. Xu, D. Thian, S. Wang, Y. Wang, F.B. Prinz, Effects of size polydispersity on electron mobility in a two-dimensional quantum-dot superlattice, Phys. Rev. B 90 (2014) 144202.
[24] Y. Liu, M. Gibbs, J. Puthussery, S. Gaik, R. Ihly, H.W. Hillhouse, M. Law, Dependence of carrier mobility on nanocrystal size and ligand length in PbSe nanocrystal solids, Nano Lett. 10 (5) (2010) 1960–1969.
[25] M.S. Kang, A. Sahu, D.J. Norris, C.D. Frisbie, Size-and temperature-dependent charge transport in PbSe nanocrystal thin films, Nano Lett. 11 (9) (2011) 3887–3892.
[26] M.S. Kang, A. Sahu, D.J. Norris, C.D. Frisbie, Size-dependent electrical transport in CdSe nanocrystal thin films, Nano Lett. 10 (9) (2010) 3727–3732.
[27] J. Wang, A. Mandelis, A. Melnikov, S. Hoogland, E.H. Sargent, Exciton lifetime broadening and distribution profiles of PbS colloidal quantum dot thin films using frequency-and temperature-scanned photocarrier radiometry, J. Phys. Chem. C 117 (44) (2013) 23333–23348.
[28] J. Wang, A. Mandelis, Variational reconstruction of exciton multipath deexcitation lifetime spectra in coupled PbS colloidal quantum dots, J. Phys. Chem. C 118 (33) (2014) 19484–19491.
[29] N. Kholmicheva, P. Moroz, E. Bastola, N. Razgoniaeva, J. Bocanegra, M. Shaughnessy, Z. Porach, D. Khon, M. Zamkov, Mapping the exciton diffusion in semiconductor nanocrystal solids, ACS Nano 9 (3) (2015) 2926–2937.
[30] J. Gao, J. Zhang, J. van de Lagemaat, J.C. Johnson, M.C. Beard, Charge generation in PbS quantum dot solar cells characterized by temperature-dependent steady-state photoluminescence, ACS Nano 8 (12) (2014) 12814–12825.
[31] J. Lee, O. Choi, E. Sim, Nonmonotonic size-dependent carrier mobility in pbse nanocrystal arrays, J. Phys. Chem. Lett. 3 (6) (2012) 714–719.
[32] B.I. Shklovskii, E.A. Efros, Electronic Properties of Doped Semiconductors, Springer, Heidelberg, 1984, p. 6.
[33] D. Yu, C. Wang, B.L. Wehrenberg, P. Guyot-Sionnest, Variable range hopping conduction in semiconductor nanocrystal solids, Phys. Rev. Lett. 92 (21) (2004) 216802.
[34] X. Lan, O. Voznyy, A. Kiani, F.P. García, de Arquer, A.S. Abbas, G.H. Kim, M. Liu, Z. Yang, G. Walters, J. Xu, M. Yuan, Z. Ning, F. Fan, P. Kanjanaboos, I. Kramer, D. Zhitomirsky, P. Lee, A. Perelgut, S. Hoogland, E.H. Sargent, Passivation using molecular halides increases quantum dot solar cell performance, Adv. Mater. 28 (2) (2016) 299–304.

[35] Z. Ning, O. Voznyy, J. Pan, S. Hoogland, V. Adinolfi, J. Xu, M. Li, A.R. Kirmani, J.P. Sun, J. Minor, K.W. Kemp, Air-stable n-type colloidal quantum dot solids, Nat. Mater. 13 (8) (2014) 822–828.

[36] B.K. Hughes, D.A. Ruddy, J.L. Blackburn, D.K. Smith, M.R. Bergren, A.J. Nozik, J.C. Johnson, M.C. Beard, Control of PbSe quantum dot surface chemistry and photophysics using an alkylselenide ligand, ACS Nano 6 (6) (2012) 5498–5506.

[37] H.E. Chappell, B.K. Hughes, M.C. Beard, A.J. Nozik, J.C. Johnson, Emission quenching in PbSe quantum dot arrays by short-term air exposure, J. Phys. Chem. Lett. 2 (8) (2011) 889–893.

[38] G.W. Guglietta, B.T. Diroll, E.A. Gaulding, J.L. Fordham, S. Li, C.B. Murray, J.B. Baxter, Lifetime, mobility, and diffusion of photoexcited carriers in ligand-exchanged lead selenide nanocrystal films measured by time-resolved terahertz spectroscopy, ACS Nano 9 (2) (2015) 1820–1828.

[39] J. Tang, K.W. Kemp, S. Hoogland, K.S. Jeong, H. Liu, L. Levina, M. Furukawa, X. Wang, R. Debnath, D. Cha, K.W. Chou, A. Fisher, A. Amassian, J.B. Asbury, E.H. Sargent, Colloidal-quantum-dot photovoltaics using atomic-ligand passivation, Nat. Mater. 10 (10) (2011) 765–771.

[40] P.R. Brown, D. Kim, R.R. Lunt, N. Zhao, M.G. Bawendi, J.C. Grossman, V. Bulovic, Energy level modification in lead sulfide quantum dot thin films through ligand exchange, ACS Nano 8 (6) (2014) 5863–5872.

[41] K.W. Johnston, A.G. Pattantyus-Abraham, J.P. Clifford, S.H. Myrskog, S. Hoogland, H. Shukla, E.J. Klem, L. Levina, E.H. Sargent, Efficient Schottky-quantum-dot photovoltaics: the roles of depletion, drift, and diffusion, Appl. Phys. Lett. 92 (12) (2008) 122111.

[42] K. Katsiev, A.H. Ip, A. Fischer, I. Tanabe, X. Zhang, A.R. Kirmani, O. Voznyy, L.R. Chou, K.W. Rollny, S.M. Thon, G.H. Carey, X. Cui, A. Amassian, P. Dowben, E.H. Sargent, O.M. Bakr, The complete in-gap electronic structure of colloidal quantum dot solids and its correlation with electronic transport and photovoltaic performance, Adv. Mater. 26 (6) (2014) 937–942.

[43] A.H. Ip, S.M. Thon, S. Hoogland, O. Voznyy, D. Zhitomirsky, R. Debnath, L. Levina, L.R. Rollny, G.H. Carey, A. Fischer, K.W. Kemp, I.J. Kramer, Z. Ning, A.J. Labelle, K.W. Chou, A. Amassian, E.H. Sargent, Hybrid passivated colloidal quantum dot solids, Nat. Nanotechnol. 7 (9) (2012) 577–582.

[44] Z. Li, F. Gao, N.C. Greenham, C.R. McNeill, Comparison of the operation of polymer/fullerene, polymer/polymer, and polymer/nanocrystal solar cells: a transient photocurrent and photovoltage study, Adv. Funct. Mater. 21 (8) (2011) 1419–1431.

[45] P. Stadler, B.R. Sutherland, Y. Ren, Z. Ning, A. Simchi, S.M. Thon, S. Hoogland, E.H. Sargent, Joint mapping of mobility and trap density in colloidal quantum dot solids, ACS Nano 7 (7) (2013) 5757–5762.

[46] S.J. Oh, N.E. Berry, J.H. Choi, E.A. Gaulding, T. Paik, S.H. Hong, C.B. Murray, C.R. Kagan, Stoichiometric control of lead chalcogenide nanocrystal solids to enhance their electronic and optoelectronic device performance, ACS Nano 7 (3) (2013) 2413–2421.

[47] D. Zhitomirsky, O. Voznyy, S. Hoogland, E.H. Sargent, Measuring charge carrier diffusion in coupled colloidal quantum dot solids, ACS Nano 7 (6) (2013) 5282–5290.

[48] A.H. Ip, A. Kiani, I.J. Kramer, O. Voznyy, H.F. Movahed, L. Levina, M.M. Adachi, S. Hoogland, E.H. Sargent, Infrared colloidal quantum dot photovoltaics via coupling enhancement and agglomeration suppression, ACS Nano 9 (9) (2015) 8833–8842.

[49] Z. Ning, X. Gong, R. Comin, G. Walters, F. Fan, O. Voznyy, E. Yassitepe, A. Buin, S. Hoogland, E.H. Sargent, Quantum-dot-in-perovskite solids, Nature 523 (7560) (2015) 324–328.

[50] Q. Sun, A. Melnikov, A. Mandelis, Quantitative self-calibrating lock-in carriero-graphic lifetime imaging of silicon wafers, Appl. Phys. Lett. 101 (24) (2012) 242107.

[51] J. Wang, A. Mandelis, A. Melnikov, Q. Sun, Trap state effects in PbS colloidal quantum dot exciton kinetics using photocarrier radiometry intensity and temperature measurements, Int. J. Thermophys. 37 (6) (2016) 1–9.

[52] H.E. Roman, L. Pavesi, Monte Carlo simulations of the recombination dynamics in porous silicon, J. Phys. Condens. Matter 8 (28) (1996) 5161.

[53] L. Turyanska, A. Patane, M. Henini, B. Hennequin, N.R. Thomas, Temperature dependence of the photoluminescence emission from thiol-capped PbS quantum dots, Appl. Phys. Lett. 90 (10) (2007) 101913.

[54] M.S. Gaponenko, A.A. Lutich, N.A. Tolstik, A.A. Onushchenko, A.M. Malyarevich, E.P. Petrov, K.V. Yumashev, Temperature-dependent photoluminescence of PbS quantum dots in glass: evidence of exciton state splitting and carrier trapping, Phys. Rev. B 82 (12) (2010) 125320.

[55] R. Kostić, M. Romčević, N. Romčević, L. Klopotowski, J. Kossut, J. Kuljanin-Jakovljević, M.I. Čomor, J.M. Nedeljković, Photoluminescence and far-infrared spectroscopy of PbS quantum dots–polyvinyl alcohol nanocomposite, Opt. Mater. 30 (7) (2008) 1177–1182.

[56] A. Mandelis, L. Hu, J. Wang, Quantitative measurements of exciton hopping transport properties in depleted-heterojunction PbS colloidal quantum dot solar cells from temperature dependent current-voltage characteristics, RSC Adv. (2016). http://dx.doi.org/10.1039/C6RA22645K.

[57] R.E. De Lamaëstre, H. Bernas, D. Pacifici, G. Franzo, F. Priolo, Evidence for a "dark exciton" state of PbS nanocrystals in a silicate glass, Appl. Phys. Lett. 88 (18) (2006) 181115.

[58] M.N. Nordin, J. Li, S.K. Clowes, R.J. Curry, Temperature dependent optical properties of PbS nanocrystals, Nanotechnology 23 (27) (2012) 275701.

[59] J. Gao, J.C. Johnson, Charge trapping in bright and dark states of coupled PbS quantum dot films, ACS Nano 6 (4) (2012) 3292–3303.

[60] A. Mandelis, J. Batista, D. Shaughnessy, Infrared photocarrier radiometry of semiconductors: physical principles, quantitative depth profilometry, and scanning imaging of deep subsurface electronic defects, Phys. Rev. B 67 (20) (2003) 205208.

[61] Z. Yang, A. Janmohamed, X. Lan, F.P. García de Arquer, O. Voznyy, E. Yassitepe, G.H. Kim, Z. Ning, X. Gong, R. Comin, E.H. Sargent, Colloidal quantum dot photovoltaics enhanced by perovskite shelling, Nano Lett. 15 (11) (2015) 7539–7543.

[62] R. Yousefi, B. Kamaluddin, Dependence of photoluminescence peaks and ZnO nanowires diameter grown on silicon substrates at different temperatures and orientations, J. Alloy. Compd. 479 (1) (2009) L11–L14.

[63] S. Tongay, J. Suh, C. Ataca, W. Fan, A. Luce, J.S. Kang, J. Liu, C. Ko, R. Raghunathanan, J. Zhou, F. Ogletree, Defects activated photoluminescence in two-dimensional semiconductors: interplay between bound, charged, and free excitons, Sci. Rep. 3 (2013) 2657.

[64] Y. Zhao, Z. Dong, S. Miao, A. Deng, J. Yang, B. Wang, Origin of deep level defect related photoluminescence in annealed InP, J. Appl. Phys. 100 (12) (2006) 123519.

[65] D. Vanmaekelbergh, P. Liljeroth, Electron-conducting quantum dot solids: novel materials based on colloidal semiconductor nanocrystals, Chem. Soc. Rev. 34 (4) (2005) 299–312.

[66] Y. Wang, J. Zhang, X.G. Zhang, H.P. Cheng, X.F. Han, First-principles study of Fe/MgO based magnetic tunnel junctions with Mg interlayers, Phys. Rev. B 82 (5) (2010) 054405.

[67] S. Datta, Electronic Transport in Mesoscopic Systems, Cambridge University Press, Cambridge, 1995.

[68] M.D. Ventra, Electrical Transport in Nanoscale Systems, Cambridge University Press, Cambridge, 2008.

[69] A.L. Efros, B.I. Shklovskii, Coulomb gap and low temperature conductivity of disordered systems, J. Phys. C: Solid State Phys. 8 (4) (1975) L49.

[70] G. Konstantatos, E.H. Sargent, PbS colloidal quantum dot photoconductive photodetectors: transport, traps, and gain, Appl. Phys. Lett. 91 (17) (2007) 173505.

[71] G. Konstantatos, L. Levina, A. Fischer, E.H. Sargent, Engineering the temporal response of photoconductive photodetectors via selective introduction of surface trap states, Nano Lett. 8 (5) (2008) 1446–1450.

[72] J.H. Warner, E. Thomsen, A.R. Watt, N.R. Heckenberg, H. Rubinsztein-Dunlop, Time-resolved photoluminescence spectroscopy of ligand-capped PbS nanocrystals, Nanotechnology 16 (2) (2004) 175.

[73] A. Kigel, M. Brumer, G. Maikov, A. Sashchiuk, E. Lifshitz, The ground-state exciton lifetime of PbSe nanocrystal quantum dots, Superlattices Microstruct. 46 (1) (2009) 272–276.

[74] D. Oron, A. Aharoni, C. de Mello, Donega, J. van Rijssel, A. Meijerink, U. Banin, Universal role of discrete acoustic phonons in the low-temperature optical emission of colloidal quantum dots, Phys. Rev. Lett. 102 (17) (2009) 177402.

[75] I. Moreels, K. Lambert, D. Smeets, D. De Muynck, T. Nollet, J.C. Martins, F. Vanhaecke, A. Vantomme, C. Delerue, G. Allan, Z. Hens, Size-dependent optical properties of colloidal PbS quantum dots, ACS Nano 3 (10) (2009) 3023–3030.

[76] G.H. Carey, L. Levina, R. Comin, O. Voznyy, E.H. Sargent, Record charge carrier diffusion length in colloidal quantum dot solids via mutual dot-to-dot surface passivation, Adv. Mater. 27 (21) (2015) 3325–3330.

[77] D.A.R. Barkhouse, A.G. Pattantyus-Abraham, L. Levina, E.H. Sargent, Thiols passivate recombination centers in colloidal quantum dots leading to enhanced photovoltaic device efficiency, ACS Nano 2 (11) (2008) 2356–2362.

[78] K.S. Jeong, J. Tang, H. Liu, J. Kim, A.W. Schaefer, K. Kemp, L. Levina, X. Wang, S. Hoogland, R. Debnath, L. Brzozowski, Enhanced mobility-lifetime products in PbS colloidal quantum dot photovoltaics, ACS Nano 6 (1) (2011) 89–99.

[79] D. Bimberg, M. Sondergeld, E. Grobe, Thermal dissociation of excitons bounds to neutral acceptors in high-purity GaAs, Phys. Rev. B 4 (10) (1971) 3451.

[80] M. Hao, J. Zhang, X.H. Zhang, S. Chua, Photoluminescence studies on InGaN/GaN multiple quantum wells with different degree of localization, Appl. Phys. Lett. 81 (27) (2002) 5129–5131.

[81] Z. Deng, Y. Jiang, Z. Ma, W. Wang, H. Jia, J. Zhou, H. Chen, A novel wavelength-adjusting method in InGaN-based light-emitting diodes, Sci. Rep. 3 (2013) 3389.

[82] M. Sebastian, J.A. Peters, C.C. Stoumpos, J. Im, S.S. Kostina, Z. Liu, M.G. Kanatzidis, A.J. Freeman, B.W. Wessels, Excitonic emissions and above-band-gap luminescence in the single-crystal perovskite semiconductors CsPbB r 3 and CsPbC l 3, Phys. Rev. B 92 (23) (2015) 235210.

[83] C.J. Youn, T.S. Jeong, M.S. Han, J.H. Kim, Optical properties of Zn-terminated ZnO bulk, J. Cryst. Growth 261 (4) (2004) 526–532.

[84] E. Cohen, R.A. Street, A. Muranevich, Bound excitons and resonant Raman scattering in $Cd_xZn_{1-x}Te$ (0.9≤x≤1), Phys. Rev. B 28 (12) (1983) 7115.

[85] K.E. Knutsen, A. Galeckas, A. Zubiaga, F. Tuomisto, G.C. Farlow, B.G. Svensson, A.Y. Kuznetsov, Zinc vacancy and oxygen interstitial in ZnO revealed by sequential annealing and electron irradiation, Phys. Rev. B 86 (12) (2012) 121203.

[86] A. Franceschetti, A. Zunger, Direct pseudopotential calculation of exciton coulomb and exchange energies in semiconductor quantum dots, Phys. Rev. Lett. 78 (5) (1997) 915.

[87] M. Liu, O. Voznyy, R. Sabatini, F.P.G. de Arquer, R. Munir, A.H. Balawi, X. Lan, F. Fan, G. Walters, A.R. Kirmani, S. Hoogland, F. Laquai, A. Amassian, E.H. Sargent, Hybrid organic-inorganic inks flatten the energy landscape in colloidal quantum dot solids, Nat. Mater. (2016). http://dx.doi.org/10.1038/nmat4800.